Molecular Mechanism of Substrate Transport and Dynamics of the Cyanobacterial Bicarbonate Transporter BicA [†]

Matthew C. Chan,[‡] Yazeed Alfawaz,[‡] and Diwakar Shukla[*,‡,¶,§,‖]

‡*Department of Chemical and Biomolecular Engineering, University of Illinois Urbana-Champaign, Urbana, IL, 61801, United States*

¶*Center for Biophysics and Quantitative Biology, University of Illinois Urbana-Champaign, Urbana, IL, 61801, United States*

§*Department of Plant Biology, University of Illinois Urbana-Champaign, Urbana, IL 61801, United States*

‖*Department of Bioengineering, University of Illinois Urbana-Champaign, Urbana, IL 61801, United States*

E-mail: diwakar@illinois.edu

[†]Running title: Transport mechanism of BicA

Abstract

Cyanobacteria are responsible for up to 80% of aquatic carbon dioxide fixation and have evolved specialized carbon concentrating mechanism to increase photosynthetic yield. As such, cyanobacteria are attractive targets for synethic biology and engineering approaches to address the demands of global energy security, food production, and climate change for an increasing world's population. The bicarbonate transporter BicA is a sodium-dependent, low-affinity, high-flux bicarbonate symporter expressed in the plasma membrane of cyanobacteria. Despite extensive biochemical characterization of BicA, including the resolution of the BicA crystal structure, the dynamic understanding of the bicarbonate mechanism remains elusive. To this end, we have collected over 1 ms of all-atom molecular dynamics simulation data of the BicA dimer to elucidate the structural rearrangements involved in the substrate transport process. We further characterized the energetics of the cooperativity between BicA promoters and investigated potential mutations that are shown to decrease the free energy barrier of conformational transitions. In all, our study illuminates a detailed mechanistic understanding of the conformational dynamics of bicarbonate transporters and provide atomistic insights to engineering these transporters for enhanced photosynthetic production.

Keywords: Bicarbonate transporter, BicA, Markov state model, SLC26, Molecular dynamics simulation, CO_2-capturing mechanisms

Introduction

Marine cyanobacteria, also known as green-blue algae, is estimated to contribute at least 30-80% of the Earth's total primary production.[1,2] In aqueous solutions, carbon dioxide (CO_2) readily interconverts between carbonic acid (H_2CO_3) and bicarbonate ions (HCO_3^-). Unlike CO_2, HCO_3^- cannot freely diffuse through the plasma membrane and thus requires specialized integral membrane transporters to accumulate inorganic carbon for photosynthe-

27 sis and carbohydrate production. Three bicarbonate transporters have been identified to be

28 ubiquitously expressed in the cyanobacteria plasma membrane: BicA, a sodium-dependent,

29 high-flux, low-affinity bicarbonate symporter; SbtA, a sodium-dependent, high-affinity sym-

30 porter, and BCT1, a four-subunit bicarbonate transporter belonging to the ATP-binding

31 cassette family[3,4] (Figure 1A). To date, the solved structure of BicA[5] (Figure 1B) and most

32 recently of SbtA[6] have illuminated the molecular architecture of the overall topology and

33 substrate binding site among these critical transporters.
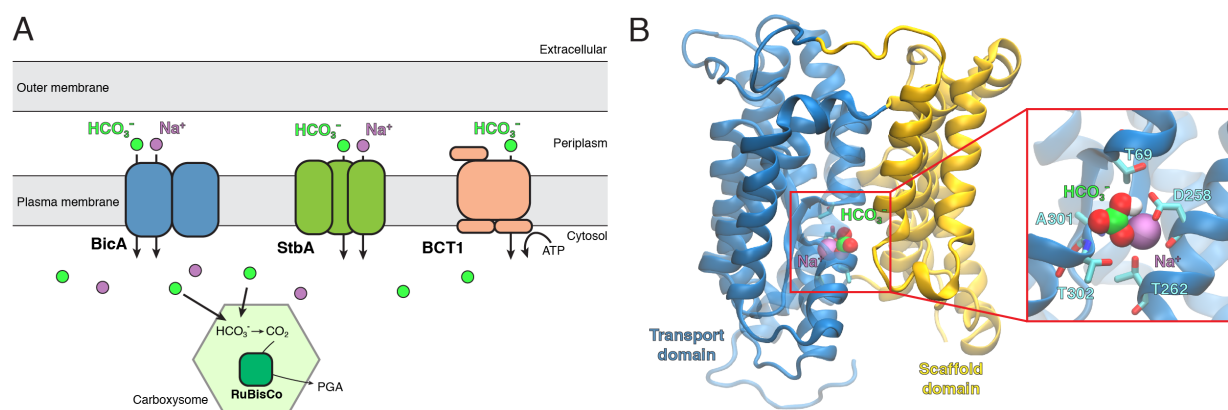
Figure 1: **Cyanobacteria bicarbonate uptake transporters.** (A) Schematic of select bicarbonate transporters expressed in the cyanobacteria plasma membrane. Transporters are depicted as follows, BicA, a sodium-dependent dimer, blue; StbA, a sodium-dependent trimer, green; BCT1, a four-subunit ATP-binding cassette transporter. Bicarbonate anions that are transported into the cytosol are then concentrated in the carboxysome, converted to carbon dioxide via carbonic anhydrase, and finally undergo photorespiration to form phosphoglyceric acid (PGA) via RuBisCo. (B) MD equilibrated structure of the BicA based on the crystal structure PDB: 6KI1. The cytoplasmic STAS domain is not shown for clarity. The transport domain and scaffold domain are colored as blue and yellow, respectively. The bound substrates are represented as spheres. Residues that coordinate the binding of the substrates are shown as sticks.

34 In C3 crops, which include rice, barley, and wheat, carbon fixation via RuBisCo (ribulose-

35 1,5-bisphosphate carboxylase/oxygenase) is notoriously known to be inefficient.[7] As such,

36 a possible approach to increases crop yield is to incorporate the efficent CO_2-capturing

37 mechanisms utilized by cyanobacteria[8] into crops. Inorganic carbon transporters are one

38 of two components that make up an effective CO_2-capturing mechanism, the other being

39 the carboxysomes, which are specialized protein micro-compartments that houses RuBisCo

3

40 and carbonic anhydrase to concentrate CO_2 for efficient carbon fixation.[9] Kinetic modeling

41 has proposed that introducing cyanobacteria bicarbonate transporters to the chloroplast of

42 C3 crops may enhance photosynthetic yield by ~10%, while adding the carboxysome system

43 may further increase yield as much as ~60%.[10] Incorporating either bicarbonate transporters

44 and the carboxysome involved the synthetic addition of foreign genes to the chloroplast of

45 plastid genome. However, whereas bicarbonate transporters are simply encoded as single

46 genes, the *in vivo* assembly of the carboxysome requires multiple proteins and presents

47 inherent difficulties to simultaneously introduce all the required genes. As such, bicarbonate

48 transporters are attractive candidates for engineering terrestrial crops to enhance inorganic

49 carbon accumulation.[11,12] Additionally, increased carbon availability promotes cyanobacteria

50 growth which may be used for the production of biofuels and other bioproducts.[13]

51 The cyanobacteria bicarbonate transporter BicA is a member of the solute carrier 26

52 (SLC26/SulP) family of anion transporters. Members of this family contain an N-terminal

53 transmembrane (TM) domain comprised of 14 helices arranged in a 7+7 inverted repeat

54 topology and a cytoplasmic C-terminal domain known as the sulfate transporter and anti-

55 sigma factor antagonist, or STAS, domain.[5] Despite low sequence conservation, transporters

56 in the SLC4 and SLC23 families share the similar 7+7 transmembrane architecture, but

57 most notably lack the STAS domain.[14] Furthermore, SLC26 transporters have been shown

58 to adopt a unique dimer interface that involves TM helices 13 and 14, whereas TM helix 6

59 forms the dimer interface for SLC4 transporters, and TM helices 5 and 12 for SLC23.[15–17]

60 Biophysical, structural, and computational studies[18–20] have illuminated the SLC26 fam-

61 ily and similar related families to adopt a canonical alternating-access model in which the

62 transporter undergoes a series of structural rearrangements to enable access of an orthosteric

63 substrate binding site from either the extracellular or intracellular side.[21] More specifically,

64 the mode of transport of SLC26 transporters has been proposed to be an elevator-like mech-

65 anism, in which helices 1-4 and 8-11 form a mobile transport domain that translates across

66 the membrane, thereby transporting substrates in and out of the cell (Figure 1B). TM he-

4

lices 5-7 and 12-14 form the scaffold domain that remains rigid and is primarily involved in oligomeric assembly. Analogous SLC26 transporters in humans are involved in the exchange of anions throughout the body and mutations in these transporters are associated with various disorders such as cystic fibrous, chloride diarrhea, and chondrodysplasia.[22]

It is estimated that by 2050, the global food production must be doubled in order to sustain a growing population.[23,24] In order to address the concern of global food security and sustainable energy, understanding the molecular mechanism of bicarbonate transport in cyanobacteria may serve as the basis for enhancing the efficiency of crop yield and biofuel production. While the resolved structure of BicA provides invaluable structural information, the conformational dynamics and energetics involved in the substrate translocation process may not be elucidated from a single structure and therefore remain elusive. With the recent surge in the computational efficiency of graphical processing units and numerical algorithms, molecular dynamics (MD) simulations combined with Markov state modeling present a robust approach to characterize complex protein dynamics at atomistic resolution.[25,26] Recent efforts in Markov state modeling have characterized the conformational heterogeneity of proteins of key interest to the plant biology community including phytohormone receptors,[27–29] and circadian clock photoreceptors.[30–32] Several membrane transporters have also been investigated using these methodologies including sugar transporters (SWEETs and SemiSWEETs),[33–35] bacterial nitrate transporters,[36] human neurotransmitter[26,37] and peptide transporters.[38] However, these transporters follow either the rocker-switch or rocking bundle mechanisms of alternate-access to facilitate the substrate transport.[39,40] BicA is distinct from these transporters because it follows the elevator-type mechanism,[41–46] where the transport domain undergoes a translation relative to the scaffold domain to achieve alternate-access required for substrate transport.[5]

In this current study, we employed long-timescale all-atom MD simulations to provide a fully atomistic and dynamic perspective into the bicarbonate transport mechanism of BicA. We further analyzed the simulation dataset using Markov state modeling[26] to quantify the

thermodynamics of the elevator-like mechanism and its associated structural rearrangements. Finally, we investigated the effects of BicA mutations on the transporter structure and dynamics and present a mechanistic basis for mutations that may be introduced to BicA to enhance bicarbonate transport activity. Overall, our computational study provides an atomistic level perspective into the molecular mechanisms of BicA bicarbonate transport which may be used for further engineering of cyanobacteria and plants.

Results and discussion

Structural characterization of a full-length BicA dimer in a cyanobacteria plasma membrane

We sought to simulate a full-length model of BicA in a lipid membrane that best resembles the physiological plasma membrane of cyanobacteria. In addition to portraying a realistic molecular environment, the increased membrane complexity may also affect thermodynamics barriers across the conformational landscape.[35] To this end, we constructed a lipid membrane based on previously characterized compositions determined for cyanobacteria (Figure 2A).[47,48] Notably, the cyanobacteria plasma membrane is comprised of mainly glycolipids. The constructed membrane consisted of the four unique and most abundant identified lipids: monogalactosyl diacylglycerol (MGDG), digalactosyl diacylglycerol (DGDG), sulfoquinovosyl diacylglycerol (SQDG), and phosphatidylglycerol (PG). The saturation of fatty acid tails were also modeled in accordance to Murata *et al.*[47] Further details of the composition of the simulated membrane are listed in Table 1.

To assess the dynamics of the cyanobacterial plasma membrane, all-atom MD simulations were performed using the AMBER18 engine[49] employing CHARMM36 force fields.[50] Three independent replicates with unique initial lipid placement were constructed and simulated for 250 ns each. The simulated membrane readily approach equilibrium after $\sim$50 ns, with an average membrane thickness of 37.2 ± 0.3 Å and area-per-lipid of 58.8 ± 0.5 Å (average

6
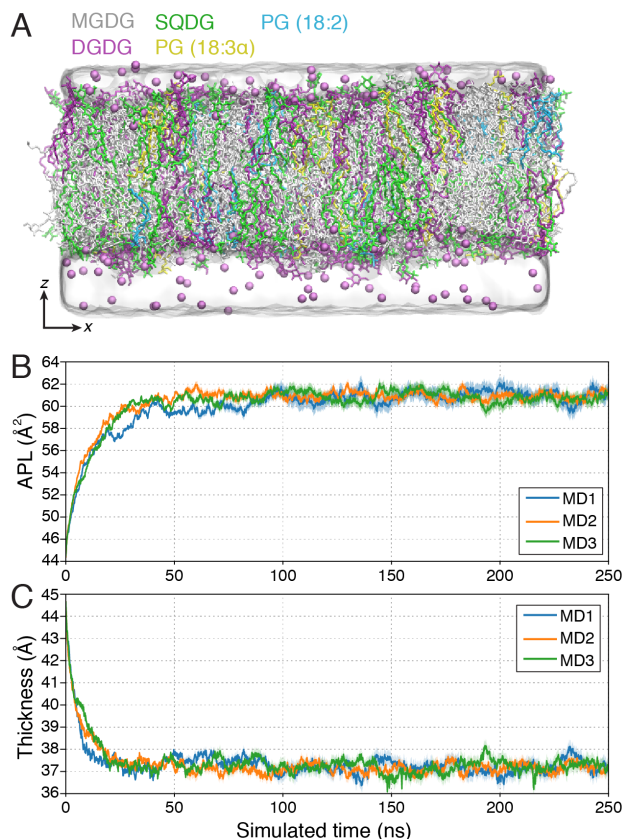
Figure 2: Molecular dynamics simulations of the cyanobacteria plasma membrane. (A) MD snapshot of the simulated cyanobacteria plasma membrane. Lipid molecules are shown as sticks and colored by individual lipid species. Sodium ions are represented as purple spheres. (B, C) Time-resolved measurements (B, area-per-lipid (APL) and C, membrane thickness) of the cyanobacteria lipid membrane. The three MD replicates are colored accordingly. Error bars represented accumulated standard deviation after the initial 50 ns.

Table 1: Composition for pure cyanobacteria plasma membrane simulations

Lipid	Saturation (sn1/sn2)	Number of lipids per leaflet	Percentage
MGDG	$18:3\gamma/16:0$	76	58%
DGDG	$18:3\gamma/16:0$	21	16%
SQDG	$18:2/16:0$	21	16%
PG	$18:2/16:0$	6	5%
PG	$18:3\alpha/16:0$	6	5%

7

119 ± standard deviation, over last 50 ns) (Figure 2B, C). We find that the physical properties

120 of our simulated membrane is in agreement with the compositionally-similar cyanobacteria

121 thylakoid membrane, previous characterized by simulation.[51]

122 With the cyanobacteria plasma membrane established, we set to construct a full-length

123 dimeric BicA system, using the resolved crystal structures of the transmembrane domain

124 (PDB: 6KI1) and the STAS domain (PDB: 6KI2).[5] Based on pulsed electron-electron dou-

125 ble resonance spectroscopy[17] and the cryo-EM structure of the dimeric SLC26a9 murine

126 transporter,[16] the initial orientation of the two BicA promoters was placed where helices 13

127 and 14 formed the interface. We alternatively modeled a full-length BicA dimer structure

128 using AlphaFold[52] and observed a similar orientation of the transmembrane domains and

129 its interface (Figure S1). However, the structure predicted by AlphaFold did not model the

130 STAS domain in accordance to the crystal structure or cryo-EM density (Figure S1). As such,

131 we proceeded with the BicA dimer structure based on the two available crystal structures

132 and superposition of other SLC26 transporters. The full-length BicA dimer was embedded

133 in the cyanobacteria plasma membrane and a total of seven MD replicates of 700 ns were

134 performed (Figure 3A). During the pre-production stages of the simulations, we observed

135 the one sodium ion to bind to one BicA monomer and remained bound throughout the 700

136 ns simulation across the seven replicates. The binding of a sodium ion to the remaining

137 BicA monomer was observed within 200-500 ns of simulation (Figure S2). In both cases, the

138 sodium ion is coordinated by the side chains of Asp258, Thr262, and Thr302, consistent with

139 the resolved crystal structure and previous mutagenesis characterization.[5] The bicarbonate

140 anion was not observed to bind in the substrate cavity within the equilibration timescales.

141 The simulations reveal that the transmembrane domains of BicA remain relatively stable

142 ($C\alpha$ RMSD < 3.5 Å), whereas the cytoplasmic STAS domain deviated from its initial struc-

143 ture ($C\alpha$ RMSD > 3.5 Å) (Figure 3B). Moreover, upon equilibrating the full-length BicA

144 system, we observed particularly the $\alpha2$ helices to unwind and propagate the collapse of the

145 domain. Indeed, the structural elements that form the STAS domain architecture are not

8
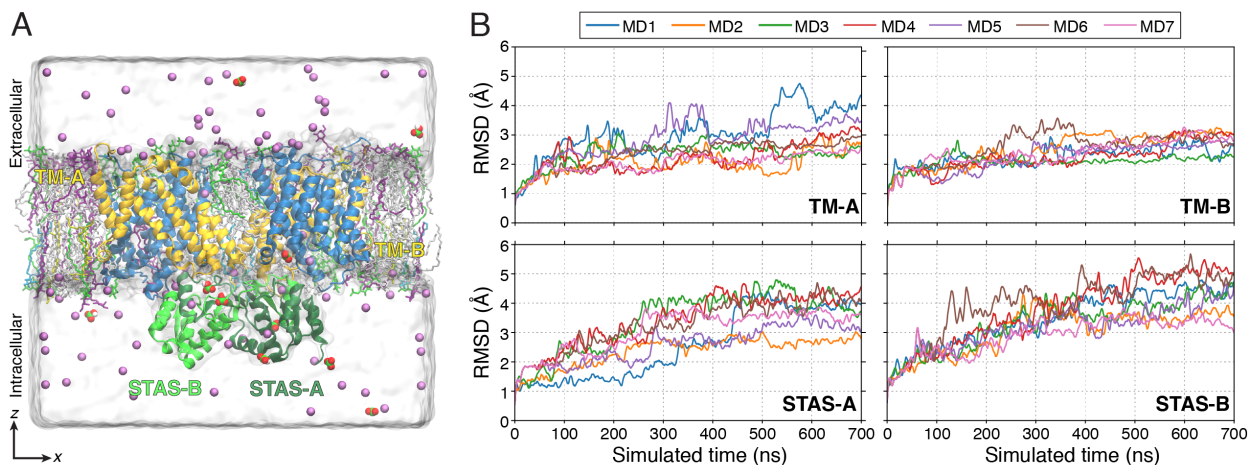
Figure 3: Stability of the full-length BicA dimer model. (A) MD snapshot of the full-length BicA dimer embedded in the cyanobacteria plasma membrane. Lipid molecules are shown as sticks and colored by lipid species as shown in Figure 2A. The BicA dimer is shown in cartoon representation and colored as follows: yellow: blue domain; blue: transport domain; green: STAS domain. Individual BicA protomers are labeled as A and B. Sodium ions are shown as purple spheres. Bicarbonate ions are shown as red and green spheres. (B) Time-resolved root mean squared deviations (RMSD) of individual BicA transmembrane (TM) and STAS domains across the 7 MD simulations. RMSD was calculated based on the starting structure of the 700 ns simulation. Individual MD replicates are colored accordingly.

maintained throughout the 700 ns long simulations (Figure S3). The inherent differences between the simulated and experimentally determined structure may be attributed to artificial crystal contacts formed during crystallography or the lack of the transmembrane domains being coexpressed to mediate the folding of the STAS domain. Functionally, the STAS domain of the sulfate transporter Sultr1;2 in *Arabidopsis thaliana* has been characterized to interact with cysteine synthase (O-acetylserine (thiol)lyase) to regulate the transporter function and mediate the cellular sulfur concentration.[53] The association of the STAS domain with other regulatory proteins is further exhibited in SLC26A3 transporter in humans with implications to cystic fibrosis.[54] As such, it is likely the STAS domain may adopt various conformations in solution and be stabilized upon association. We further simulated a BicA dimer with the STAS domains removed and did not observe difference in dimer stability of the transmembrane domain (Figure S4). In all, the simulations suggest that the STAS

9

domain does not provide additional structural stability in the membrane and is concluded to be more involved in regulatory mechanisms.

Structural requirements and energetics of BicA conformational transitions

As the timescales of large structural rearrangements and substrate transport may occur on the orders of microseconds or greater,[55,56] observing these long timescale processes through conventional MD approaches may present inherent challenges in achieving adequate conformational sampling. As such, to simulate the bicarbonate transport process of BicA, we implemented a Markov state model (MSM) based adaptive sampling scheme to maximize the exploration of the conformational landscape.[26] In brief, the adaptive sampling protocol is an iterative approach in which multiple simulations are conducted in parallel and then clustered using a K-means algorithm based on geometric criteria. To sampling the BicA substrate translocation process, the distances between substrates and binding site and the z-component of the transport domain were chosen as the adaptive sampling metrics. To maximize the likelihood of exploring new conformations, structures from the least populated states are seeded for the subsequent round of simulation. Furthermore, to expedite the sampling, we seeded simulations from a targeted MD trajectory in which captured the transition from inward-facing to outward-facing (Figure S5). A total of 1.003 millisecond of aggregate simulation data were collected and used to construct a MSM.[57] We note that the conformational sampling performed for this study simulates the export of bicarbonate to the extracellular side. Though BicA is responsible for concentrating inorganic carbon in the cell, the benefit of the Markov state modeling is representing the transport process as a reversible process and calculating the reversible transition probabilities between states, thereby capturing the bicarbonate import process.

By projecting the MSM-weighted simulation data on the reaction coordinates defined by the z-component of the Asp258 Cα atom (the residue that coordinates binding of the

10
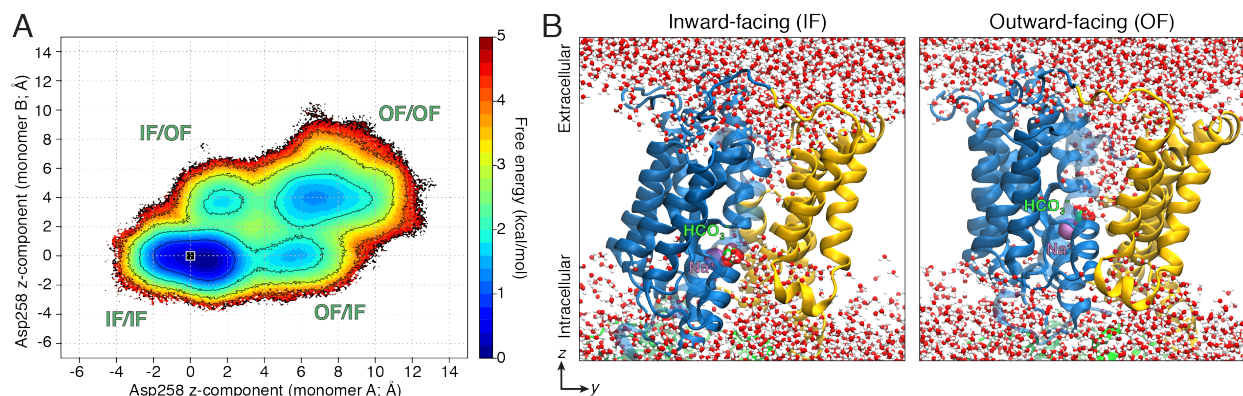
Figure 4: Energetics of BicA conformational transitions. (A) MSM-weighted conformational free energy landscape of BicA. The simulation data are projected on the axis defined by the z-component of the Cα atom of Asp258 for the respective BicA protomers. The displacement of Asp258 is measured with respected to the initial structure used for adaptive sampling simulations and indicated by the black square. Standard error measurement of the free energy landscape is presented in Figure S6. (B) Representative MD snapshots of BicA showing the solvent accessibility of the substrate binding site in the inward-facing (IF) and outward-facing (OF) conformation. The transport domain is shown as blue cartoon, while the scaffold domain is colored in yellow. Water molecules are shown as red and white spheres.

184 bicarbonate anion, Figure 1B), the conformational free energy landscape illustrates the co-

185 operativity of the two BicA protomers (Figure 4A). Inward-facing conformations, in which

186 the substrate binding site is accessible from the intracellular solvent (Figure 4B), are ener-

187 getically stable with a relative free energy of 0-1 kcal/mol. Furthermore, the simulations

188 reveal that the BicA protomer may independently undergo structural rearrangements to

189 form outward-facing states in which the transport domain has shifted ∼6Å and the sub-

190 strate binding site is now accessible to the extracellular space (Figure 4B). The free energy

191 barrier associated with transitions from the inward-facing to outward-facing for a single

192 BicA protomer is estimated to be ∼2.5-3 kcal/mol (Figure 4A, S7). Based on the sampling

193 seeded from the targeted MD trajectory, structures in which both BicA protomers form the

194 outward-facing conformation are stable with a relative free energy minima of ∼2 kcal/mol.

195 However, the transition free energy barriers for the remaining BicA protomer to adopt the

196 outward-facing state, given that the other protomer is already outward-facing, is ∼3-4 kcal/-

11

197 mol. Likewise, for both protomers to simultaneously transition to the outward-facing state

198 is energetically less favored with free energy barriers of ∼4-5 kcal/mol (Figure S7). Overall,

199 the conformational free energy landscape suggest one protomer of BicA actively undergoes

200 structural transitions in the dimeric state, consistent with previous studies of the SLC26Dg

201 fumarate transporter.[18]

202 We note the presence of two proline residues, Pro122 and Pro341, that flank the transport

203 domain (Figure 5A). Sequence analysis reveals that in 300 homologs, Pro341 is absolutely

204 conserved whereas Pro122 is substituted for Ser in a few homologs (Figure 5B). As the

205 proline residue adopts a cyclic side chain that uniquely constrains the protein backbone,

206 we hypothesized if the steric effects provide the structural requirements for the conforma-

207 tional transitions of BicA. To investigate the effects of the proline residues on the transport

208 dynamics, we implemented umbrella sampling simulations and calculated the potentials of

209 mean force (PMF) profiles of BicA to transition from inward-facing to outward-facing. The

210 conformational free energy landscape suggest that a single BicA protomer is more favored

211 to transition rather than both simultaneously. As such, umbrella sampling simulations were

212 initiated from MD snapshots of the BicA monomer A obtained from the adaptive sampling

213 simulations. Umbrella sampling simulations were conducted with the NAMD2.14 package.[58]

214 In the wild-type BicA system, the highest free energy barrier is associated with the

215 transition to the outward-facing state, with a barrier of 3.97 ± 0.24 kcal/mol. When the

216 Pro122 and Pro341 are mutated to glycine residues (Pro122Gly;Pro341Gly), we observed

217 the stability of the outward-facing state to be similar to that of the wild-type (wild-type:

218 3.39 ± 0.25 kcal/mol, Pro122Gly;Pro341Gly: 3.66 ± 0.24 kcal/mol), but the free energy

219 barrier has now increased to 4.81 ± 0.21 kcal/mol (Figure 5C). Contrary to prolines, glycine

220 residues provide innate flexibility of the peptide backbone given the lack of a heavy atom

221 side chain. However, such flexibility did not provide necessary structural requirements to

222 promote the formation of the outward-facing state. We further simulated and calculated

223 the PMF profile for the respective alanine mutant (Pro112Ala;Pro341Ala) and observed
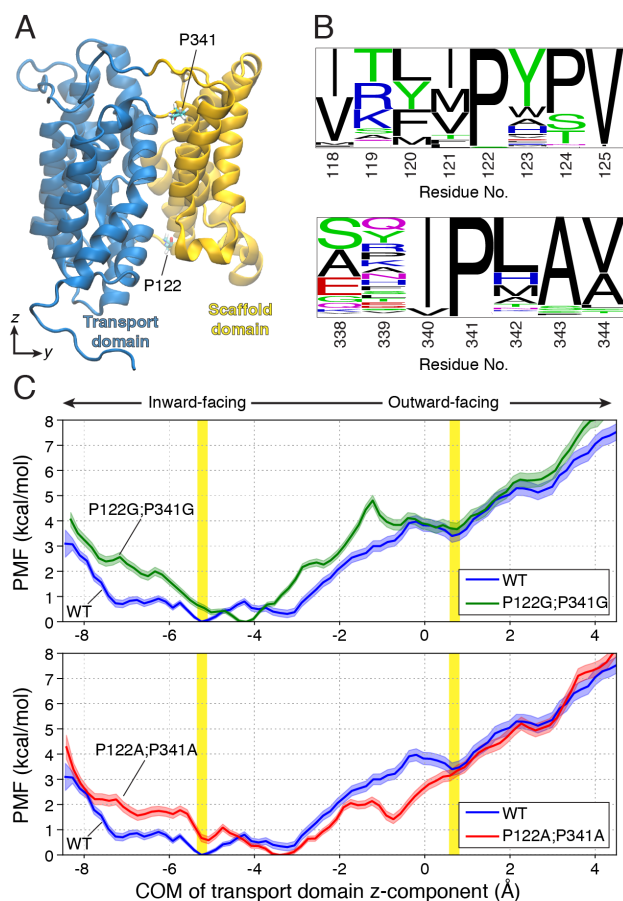
Figure 5: Conserved prolines residues flank the BicA transport domain. (A) Structure of the transmembrane domain of BicA, colored by transport and scaffold domain in blue and yellow respectively. Proline residues, P122 and P341, investigated are indicated and shown as sticks. (B) Sequence logo representation[59] of the proline and adjacent residues depicting the amino acid frequency of 300 homologs. Size of the amino acid font represents its respective frequency in the multiple sequence alignment. (C) Potentials of mean force (PMF) profiles for inward-facing to outward-facing transitions of wild-type (WT) and mutant BicA. BicA systems are colored as follows, wild-type: blue, P122G;P341G: green, P122A;P341A: red. x-axis represents the z-coordinate displacement of the center of mass (COM) of the transport domain with respect to the center of mass of the scaffold domain. Inward- and outward-facing conformations are highlight as vertical yellow bars.

that the free energy barrier are reduced to 2.14 ± 0.16 kcal/mol (Figure 5C). Moreover,

the Pro112Ala;Pro341Ala mutant stabilizes an intermediate outward-facing state, but the

complete outward-facing state remains of similar stability (wild-type: 3.39 ± 0.25 kcal/mol,

Pro122Ala;Pro341Ala: 3.15 ± 0.21 kcal/mol). As alanine residues enable more structural

13

constraints on the backbone compared to the glycine residues, the PMF profiles suggest that unique dihedral constraints provided by proline residues facilitates the necessary structural rearrangements of the transport domain of BicA, although we cannot comment on how these mutants may affect transporter expression, biogenesis, folding, or stability.

Hydrophobic interactions mediate closure of the transport domain

Membrane transporters adopt a canonical series of structural rearrangements that facilitates proper substrate transport across the membrane, otherwise known as the alternating access mechanism.[60] As such, the substrate binding site is accessible to either the intracellular or extracellular space at a given time. Simulations of BicA reveals that the closure of the transporter from either side is facilitated by hydrophobic residues that line the substrate translocation pathway (Figure 6). Specifically, in the inward-facing conformation, closure from the extracellular side is primarily mediated by transmembrane helices 1 and 3 of the transport domain and helices 5, 7, 12, and 14 of the scaffold domain (Figure 6A). Upon substrate transport, as the transport domain shifts across the membrane, intracellular gate is formed by residues on helices 8 and 10 with the scaffold domain (Figure 6B). As per the elevator-like mechanism, the scaffold domain serves as a shared gate between intracellular and extracellular residues. Furthermore, residues that comprise the hydrophobic gate are generally conserved among other transporters that adopt the 7+7 transmembrane helix topology (Figure S8, S9). We expect that the hydrophobic residues in the respective positions of SLC4 and SLC23 transporters to adopt a similar role in regulating the opening and closure of the transporter.

Given that the molecular gates of BicA are primarily facilitated by the hydrophobic interactions of aliphatic side chains, we sought to determine if mutations may be introduced to increase the substrate transport rate. Specifically, we hypothesized if substitutions to alanine residues may decrease the contacting surface area, while still retaining the nonpolar local environment to maintain proper transport function. To this end, we targeted residues

14
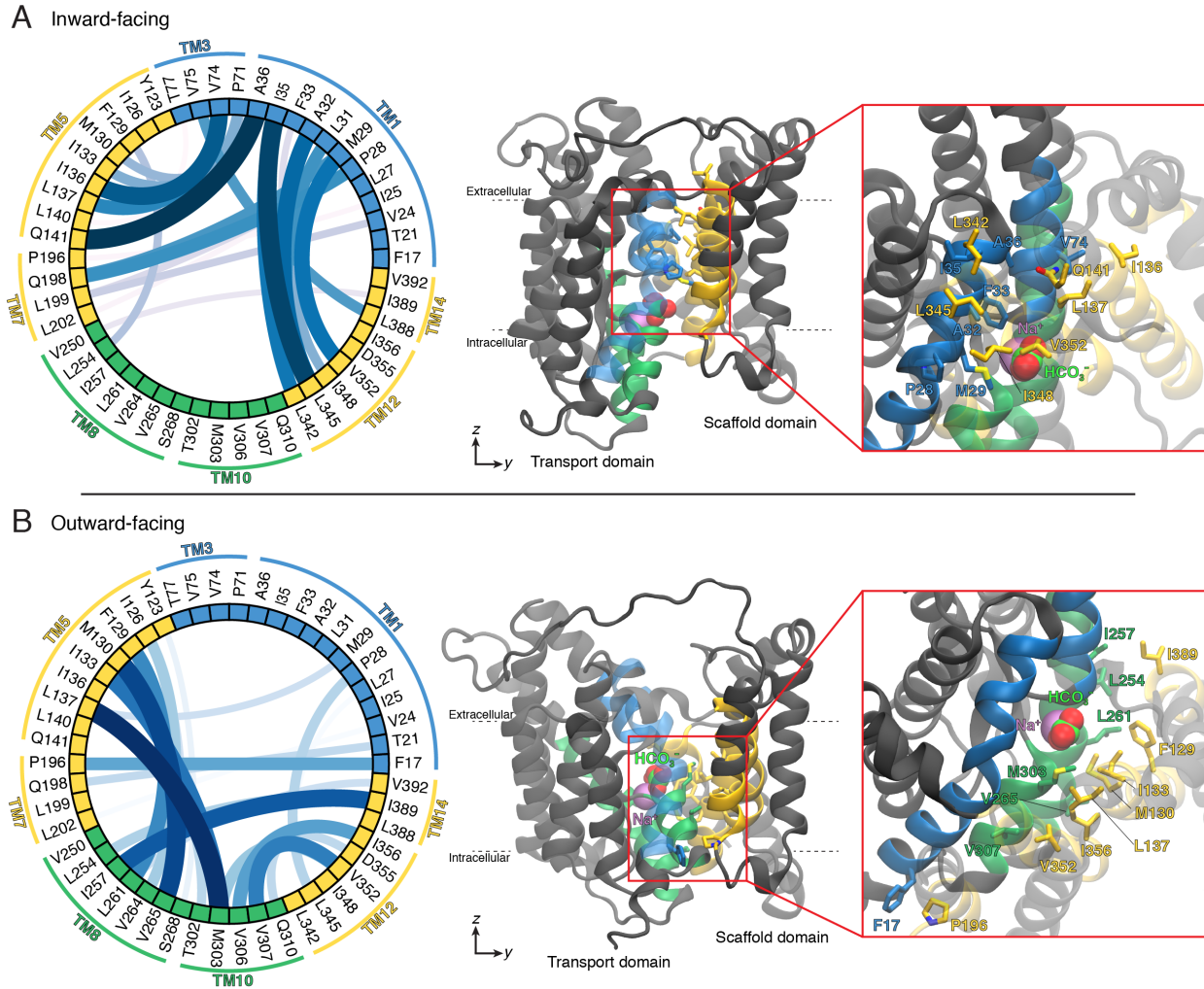
Figure 6: Hydrophobic gating residues of BicA. Chord diagram depicting the probability of interactions formed between gating residues in the (A) inward-facing conformation and (B) outward-facing conformation. Probability of interactions were calculated on 50,000 MD structures drawn from the respective free energy basin. Thickness and color intensity of connections between nodes represent the relative probability between two residues interacting. Accompanying MD snapshot showing selected residues mediating the closure of the transporter. Transmembrane (TM) helices are colored as follows, TM1, TM3: blue; TM5, TM7, TM12, TM14: yellow; TM8, TM10: green.

with large aliphatic side chains (Met, Leu, Ile, etc) located on various gating helices of BicA and residues of high contact probability based on the MD simulations. Three BicA triple mutants were simulated via the umbrella sampling protocol to delineate its effects on the energetics of the transporter conformational dynamics.

We first characterized mutations of residues on the hydrophobic gate that re-

15
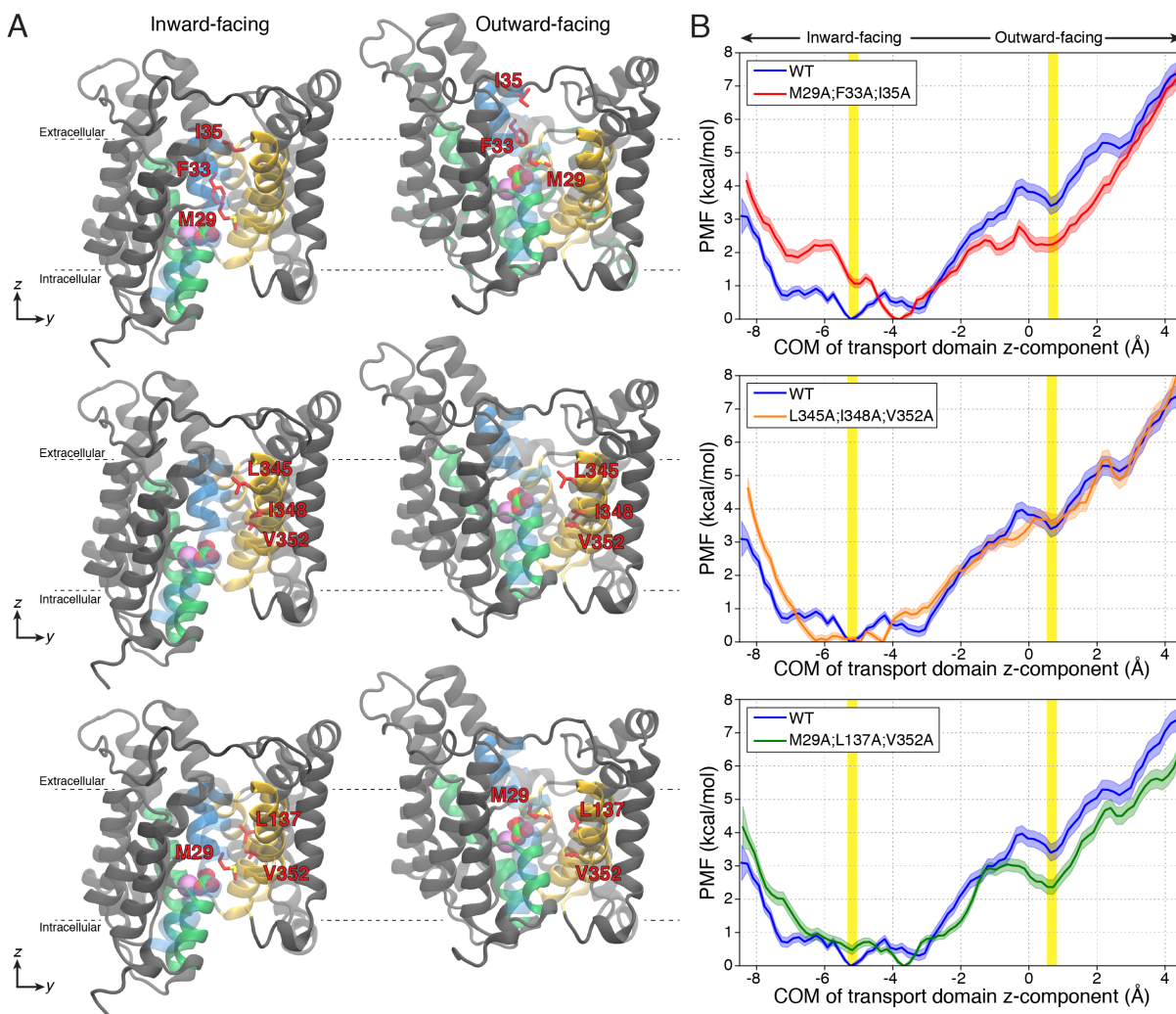
Figure 7: Simulated BicA triple mutants. (A) MD snapshots of the inward-facing and outward-facing conformations of BicA. Mutated residues are shown as sticks and colored red. The bicarbonate and sodium ion are shown as spheres and colored green and purple, respectively. Transmembrane (TM) helices are colored as follows, TM1, TM3: blue; TM5, TM7, TM12, TM14: yellow; TM8, TM10: green. The mutants investigated in this study are Met29Ala;Phe33Ala;Ile35Ala (top), Leu345Ala;Ile348Ala;Val352Ala (middle), and Met29Ala;Leu137Ala,Val352Ala (bottom). (B) Potential of mean force (PMF) profiles of the three studied BicA triple mutants. The wild-type BicA is shown in blue and duplicated for comparison. BicA systems are colored as follows, wild-type: blue, Met29Ala;Phe33Ala;Ile35Ala: red, Leu345Ala;Ile348Ala;Val352Ala: orange, Met29Ala;Leu137Ala,Val352Ala: green. x-axis represents the z-coordinate displacement of the center of mass (COM) of the transport domain with respect to the center of mass of the scaffold domain. Inward- and outward-facing conformations are highlight as vertical yellow bars.

16

259 side on the transport domain. The BicA triple mutant containing the substitutions

260 Met29Ala;Phe33Ala;Ile35Ala are located on the extracellular half of transmembrane helix

261 1 (Figure 7, top). These residues were primarily found to interact with residues on TM12

262 to restrict access from the extracellular space and stabilize the inward-facing conformation

263 (Figure 6A). The PMF profile of the Met29Ala;Phe33Ala;Ile35Ala BicA mutant reveals the

264 free energy barrier to form the outward-facing state has decreased to 2.78 ± 0.20 kcal/mol,

265 as compared to the 3.97 ± 0.24 kcal/mol in wild-type BicA (Figure 7, top). Furthermore, the

266 relative free energy barrier of outward-facing to inward-facing transitions remains similar to

267 the wild-type (Met29Ala;Phe33Ala;Ile35Ala: 0.56 kcal/mol, wildtype: 0.58 kcal/mol) consis-

268 tent that these residues are primarily responsible for extracellular closure and not predicted

269 to directly affect the stability of the outward-facing conformation.

270 The residues of the second BicA triple mutant, Leu345Ala;Ile348Ala;Val352Ala, are lo-

271 cated on transmembrane helix 12 of the scaffold domain (Figure 7, middle). The PMF pro-

272 files for Leu345Ala;Ile348Ala;Val352Ala predicts a modest decrease in the free energy barrier

273 (Leu345Ala;Ile348Ala;Val352Ala: 3.72 ± 0.24 kcal/mol, wild-type: 3.97 ± 0.24 kcal/mol),

274 however the outward-facing state is further destabilized. We suspect as transmembrane he-

275 lix 12 serves as a shared gating helix that facilitate both inward-facing and outward-facing

276 conformations, contributes to a slight favorable reduction in the free energy barrier, but also

277 compromises on the destabilized interactions that close the intracellular pathway.

278 Lastly, the BicA mutant Met29Ala;Leu137Ala,Val352Ala targets residues on both the

279 transport and scaffold domain (Figure 7, bottom). This mutant was specifically simu-

280 lated to remove the hydrophobic interactions involving Met29. In the inward-facing state,

281 Met29 interacts with Val352, whereas in the outward-facing state Met29 switches its in-

282 teraction partner to Leu137 (Figure 6). Similar to the first described BicA triple mutant

283 (Met29Ala;Phe33Ala;Ile35Ala), the PMF profile delineates a decrease in the free energy bar-

284 rier (Met29Ala;Leu137Ala,Val352Ala: 3.05 ± 0.19 kcal/mol, wild-type: 3.97 ± 0.24 kcal/-

285 mol) and similar stability of the outward-facing state. Overall, our simulations predict

alanine substitutions to residues on the transmembrane domain, specifically transmembrane helix 1, decrease the free energy barriers for structural rearragements to increase bicarbonate uptake.

Conclusions

Bicarbonate transporters are key membrane transporters that regulate photosynthesis production. In this study, we utilized adaptive sampling and Markov state modeling to characterize the structural dynamics and thermodynamics of the BicA transport mechanism. Our simulations reveal that BicA protomers are more favored to undergo conformational transitions independently rather than simultaneously, consistent with previous cross-linking studies of the SLC26Dg transporter.[17] In our simulations, we observed the cytoplasmic STAS domain does not remain stable in solution and undergo various structural rearrangements. We hypothesized, the stability of the STAS domain may be facilitated with other association proteins *in vivo*. Previous experimental characterization of the related *E. coli* YchM transporter has suggested the STAS domain to interact with a number of regulatory proteins with implications on transport activity.[61] Further studies may focus on *in vivo* regulatory mechanisms of BicA.

We further investigated various BicA mutants that are predicted to affect the conformational energetics of the transport process. We predict that the unique steric constraints on the protein backbone provided by prolines residues located at junction of the scaffold and transport domain facilitate the proper conformational dynamics for transport. Furthermore, substitutions to bulky aliphatic residues that form the hydrophobic gate decrease the free energy barriers for inward-facing to outward-facing transitions. Specifically, alanine mutations located on transmembrane helix 1 are predicted to enhance transport with minimal consequences on the stability of conformations. Such mutations to the hydrophobic gating residues introduced to the sodium/proton antiporter PaNhaP were also identified to in-

311 crease transport activity.[62] However, how these mutations may affect transporter expression,

312 folding, trafficking, or biogenesis cannot be delineated from simulations. In all, the exten-

313 sive simulations conducted in this study provide a comprehensive mechanistic view of BicA

314 transport dynamics and elucidate potential engineered mutations to enhance cyanobacteria

315 photosynthetic yield.

Methods

MD simulations of pure cyanobacteria plasma membrane

318 To characterize the structural dynamics of BicA, we first sought to model a physiological

319 membrane environment. Based on previous experimental characterization of cyanobacte-

320 ria membranes, we constructed a symmetric lipid membrane containing the monogalactosyl

321 diacylglycerol (MGDG), digalactosyl diacylglycerol (DGDG), sulfoquinovosyl diacylglycerol

322 (SQDG), and phosphatidylglycerol (PG). The total number of each lipid species and lipid

323 tail saturation are detailed in Table 1. A total of 130 lipid molecules per leaflet were assem-

324 bled using PACKMOL.[63] Water molecules and sodium ions to neutrailze the system were

325 further added. In all, the final MD membrane system contained 152 MGDG molecules, 42

326 DGDG molecules, 42 SQDG molecules, 24 PG molecules, 152 sodium ions, and 19,998 water

327 molecules totaling 140,834 atoms in a rectilinear box of 140 x 101 x 105 Å^3. A total of three

328 membrane systems, randomizing the initial lipid placement, were constructed.

329 The MD systems were parameterized using the CHARMM36m force field. The param-

330 eters for the saturated lipids tails (18:3γ/16:0, 18:2/16:0, 18:3α/16:0), which are not orig-

331 inally parameterized in CHARMM36, were derived analogous from parameters of related

332 lipid molecules in the CHARMM36 molecule set. The *psf* topology and coordinating file

333 were created using the VMD psfgen plugin and converted to AMBER *prmtop* topology and

334 *rst7* coordinate files using the *chamber* module of the ParmEd package.

335 Simulations were performed on the AMBER18 package using the *pmemd* GPU acceler-

ated module. The MD system was first minimized 7,000 steps using the steepest descent method followed by 93,000 steps using the conjugate gradient method. Prior to production simulations, the system was heated to 300K in 100K increments for 1 ns each while restraining the lipid head group atoms with a force constant of 1 kcal/mol-$Å^2$. Production simulations were performed in an NPT ensemble using Langevin dynamics with a damping coefficient of 1 ps^{-1} at 300K, 1 bar, and positional restraints removed. A Monte Carlo barostat with an update interval of 100 steps was used to maintain pressure. A 12 distance cutoff was applied to calculate nonbonded interactions. Long-range electrostatic interactions were treated with the Particle mesh Ewald method. Hydrogen bonds were constrained using the SHAKE algorithm. An integration timestep of 2 fs was used for membrane simulations. Each MD replicate was simulated for 250 ns with a trajectory frame saving rate of 100 ps.

Modeling of the full-length BicA dimer system

The three-dimensional coordinates of the resolved BicA crystal structure (PDB:6KI1, 6KI2)[5] were used as the starting structure for simulations. First, transmembrane helix 14 was modelled based on the SLC26Dg structure (PDB: 5DA0) To model the full-length BicA dimer, two transmembrane domains were aligned to the SLC26a9 murine transporter,[16] in which transmembrane helices 13 and 14 formed the dimeric interface.[17] The STAS domain was placed under the transmembrane domain and residues that linked the two domains were modelled with MODELLER.[64] We found that the resulting full-length BicA dimer to modestly fit in the cryo-EM map,[5] which may be attributed to its low-resolution or reconstruction in detergent which may impact the packing of membrane proteins. The modelled dimer, containing residues 2-547, was embedded in the cyanobacteria plasma membrane and solvated with TIP3P water molecules. 10 bicarbonate anions were randomly placed in the solvent and sodium ions were added to neutralize the system. The final BicA dimer system consisted of 2 BicA protomers, 152 MGDG molecules, 42 DGDG molecules, 42 SQDG molecules, 24 PG molecules, 10 bicarbonate anions, 80 sodium ions, and 30,200 water molecules totaling

20

362 in 141,886 atoms in a rectilinear box of 140.0 x 101.0 x 126.0 Å^3.

363 The alternative structure prediction of the BicA dimer was generated using Al-
364 phaFold v2.2.0 in tandem with the multimer mode.[52,65] The AlphaFold prediction
365 was performed using the following parameters: `--max_template_date=2022-05-01`,
366 `model_preset=multimer, --norun_relax, --db_preset=reduced_dbs`. The output
367 structure from AlphaFold was not used for simulations in this study.

MD simulations of full-length BicA dimer

369 The BicA dimer system was parameterized using the CHARMM36m force field and con-
370 ducted on the AMBER18 package. Prior to production simulation, the system was mini-
371 mized for 5,000 steps using the steepest descent method, followed by 45,000 steps using the
372 conjugate gradient method. The BicA dimer was then subjected to 10 pre-production sim-
373 ulations with varying atoms restrained, totaling in 150 ns. A detailed list of temperatures,
374 restrained atoms, and simulation length for each pre-production step is presented in Table
375 S1.

376 Production simulations were performed under the same conditions and parameters as the
377 previous described pure membrane system, with the exception of the use of a 4 fs integration
378 timestep and hydrogen mass repartition.[66] To determine the stability of the full-length BicA
379 dimer, a total of 7 simulations were initiated from the last pre-production step and simulated
380 for 700 ns. The resulting trajectories from these simulations yielded BicA to remain in the
381 inward-facing state. As such, to explore the conformational space of BicA, we adaptively
382 sampled the conformational landscape based on the distances of the substrate to the binding
383 sites and the displacement of the transport domain.[26] After 14 rounds of adaptive sampling,
384 we did not observe either BicA protomer to transition from the inward-facing state (Fig-
385 ure S10). As such, we seeded subsequent rounds from a targeted MD trajectory in which
386 simulated the transition from inward-facing to outward-facing (Figure S5). The targeted
387 MD simulation was performed using NAMD2.14[58] using a 200 kcal/mol-Å^2 force constant

21

388 and an outward-facing/outward-facing BicA homology model based on the NBCe1 cryo-EM

389 structure (PDB: 6CAA)[67] as the target structure. A total of 29 adaptive rounds, in which

390 individual trajectories were 60 ns long, were conducted and totaled in 1.003 ms of aggregate

391 simulation data (Table S2).

Trajectory analysis

393 Trajectories were processed with in-house scripts utilizing the CPPTRAJ, pytraj,[68] and

394 MDTraj[69] packages. Simulation trajectories were visualized using Visual Molecular Dy-

395 namics (VMD) 1.9.3.[70] Residue contact probabilities were calculated using the GetContacts

396 (https://getcontacts.github.io/) python package.

Markov state modeling

398 All 1.003 ms of aggregate simulation data from adaptive sampling simulations were used

399 to construct a Markov state model (MSM). The simulation data were featurized based on

400 the distances of residue pairs that were identified to uniquely formed in the inward- and

401 outward-facing states and determined using a residue-residue contact score (RRCS).[71] In all,

402 192 distances were identified between the two BicA protomers (Table S3). Additionally, the

403 z-components of Asp258 and the transported bicarbonate anion were included as features for

404 the MSM, totaling in 196 cartesian features. The number of time-independent components

405 (tICs) and number of clusters was optimized using a grid search to maximize the VAMP1

406 score (Figure S11A). The best-scoring model was achieved with 10 tICs and 400 clusters.

407 A lagtime of 10 ns was determined based on convergence of the implied timescales (Figure

408 S11B).

Umbrella sampling simulations

To investigate the energetics of conformational transitions of BicA mutants, we employed umbrella sampling The displacement between the z-component of the transport domain center of mass and the z-component of the scaffold domain center of mass was used as the reaction coordinate to describe the conformational transitions from inward-facing to outward-facing. Based on the conformational free energy landscape, one protomer of BicA is predicted to undergo transitions at once, and as such, we employed the umbrella sampling protocol on only BicA monomer A. Structures were drawn from the conformational landscape. A total of 26 windows from z-coordinates -8.0 to +4.5, in 0.5Å intervals were used to seed umbrella sampling simulations. Each window was simulated for 9 ns. Umbrella sampling simulations were performed using NAMD2.14[58] using a 2 fs integration timestep, 12Å cutoff with a 10Å switching distance, and a harmonic force constant of 15 kcal/mol-Å^2. Simulation frames were saved every 10 ps. Potentials of mean force (PMFs) were calculated using the multistate Bennett acceptance ratio as implimented by the pyMBAR python package.[72]

Generation of multiple sequence alignments

Multiple sequence alignments were generated using the ConSurf web server.[73] The sequences of BicA, UraA (PDB:5XLS),[18] and NCBe1 (PBD:6CAA)[67] were used as input to represent SLC26, SLC23, and SLC4 families. A 95% maximal identity between sequences and a 35% minimal identity between homologs was used to created the alignment. 300 represented sequences were sampled from the list of accepted homologs. Sequence logo figures were generated using the WebLogo server.[59]

Data availability

Molecular dynamics trajectories generated in this study are not publicly deposited as it is over 4 TB in size. Datasets are available upon request and may require several business days

433 to share. Once provided, we do not enforce any limitation for how the data may be used

434 once requested and shared.

Acknowledgement

436 This research was part of the Blue Waters sustained-petascale computing project, which was

437 supported by the National Science Foundation (awards OCI-0725070 and ACI-1238993) the

438 State of Illinois, and as of December, 2019, the National Geospatial-Intelligence Agency. Blue

439 Waters was a joint effort of the University of Illinois Urbana-Champaign and its National

440 Center for Supercomputing Applications.

Author contributions

442 M.C.C. and D.S. designed the study. D.S. supervised the study. M.C.C. and Y.A. performed

443 simulations. M.C.C., Y.A., and D.S. analyzed data. M.C.C. wrote manuscript with input

444 from D.S.

Funding

446 This work was funded by NSF MCB 18-45606 to D.S.

Conflicts of interest

448 The authors declare that they have no conflicts of interest with the contents of this article.

References

(1) Liu, H.; Nolla, H. A.; Campbell, L. Prochlorococcus growth rate and contribution to primary production in the equatorial and subtropical North Pacific Ocean. *Aquatic Microbial Ecology* **1997**, *12*, 39–47.

(2) Partensky, F.; Hess, W. R.; Vaulot, D. Prochlorococcus, a marine photosynthetic prokaryote of global significance. *Microbiology and molecular biology reviews* **1999**, *63*, 106–127.

(3) Price, G. D.; Woodger, F. J.; Badger, M. R.; Howitt, S. M.; Tucker, L. Identification of a SulP-type bicarbonate transporter in marine cyanobacteria. *Proceedings of the National Academy of Sciences* **2004**, *101*, 18228–18233.

(4) Price, G. D. Inorganic carbon transporters of the cyanobacterial CO 2 concentrating mechanism. *Photosynthesis research* **2011**, *109*, 47–57.

(5) Wang, C.; Sun, B.; Zhang, X.; Huang, X.; Zhang, M.; Guo, H.; Chen, X.; Huang, F.; Chen, T.; Mi, H.; Yu, F.; Liu, L.-N.; Zhang, P. Structural mechanism of the active bicarbonate transporter from cyanobacteria. *Nature Plants* **2019**, *5*, 1184–1193.

(6) Liu, X.-Y.; Hou, W.-T.; Wang, L.; Li, B.; Chen, Y.; Chen, Y.; Jiang, Y.-L.; Zhou, C.-Z. Structures of cyanobacterial bicarbonate transporter SbtA and its complex with PII-like SbtB. *Cell Discovery* **2021**, *7*, 1–5.

(7) Bracher, A.; Whitney, S. M.; Hartl, F. U.; Hayer-Hartl, M. Biogenesis and metabolic maintenance of Rubisco. *Annual review of plant biology* **2017**, *68*, 29–60.

(8) Rae, B. D.; Long, B. M.; Förster, B.; Nguyen, N. D.; Velanis, C. N.; Atkinson, N.; Hee, W. Y.; Mukherjee, B.; Price, G. D.; McCormick, A. J. Progress and challenges of engineering a biophysical CO2-concentrating mechanism into higher plants. *Journal of Experimental Botany* **2017**, *68*, 3717–3737.

(9) Badger, M. R.; Price, G. D. CO2 concentrating mechanisms in cyanobacteria: molecular components, their diversity and evolution. *Journal of experimental botany* **2003**, *54*, 609–622.

(10) McGrath, J. M.; Long, S. P. Can the cyanobacterial carbon-concentrating mechanism increase photosynthesis in crop species? A theoretical analysis. *Plant physiology* **2014**, *164*, 2247–2261.

(11) Du, J.; Förster, B.; Rourke, L.; Howitt, S. M.; Price, G. D. Characterisation of cyanobacterial bicarbonate transporters in E. coli shows that SbtA homologs are functional in this heterologous expression system. *PloS one* **2014**, *9*, e115905.

(12) Rolland, V.; Badger, M. R.; Price, G. D. Redirecting the cyanobacterial bicarbonate transporters BicA and SbtA to the chloroplast envelope: soluble and membrane cargos need different chloroplast targeting signals in plants. *Frontiers in plant science* **2016**, *7*, 185.

(13) Gupta, J. K.; Rai, P.; Jain, K. K.; Srivastava, S. Overexpression of bicarbonate transporters in the marine cyanobacterium Synechococcus sp. PCC 7002 increases growth rate and glycogen accumulation. *Biotechnology for biofuels* **2020**, *13*, 1–12.

(14) Chang, Y.-N.; Geertsma, E. R. The novel class of seven transmembrane segment inverted repeat carriers. *Biological Chemistry* **2017**, *398*, 165–174.

(15) Gorbunov, D.; Sturlese, M.; Nies, F.; Kluge, M.; Bellanda, M.; Battistutta, R.; Oliver, D. Molecular architecture and the structural basis for anion interaction in prestin and SLC26 transporters. *Nature communications* **2014**, *5*, 3622.

(16) Walter, J. D.; Sawicka, M.; Dutzler, R. Cryo-EM structures and functional characterization of murine Slc26a9 reveal mechanism of uncoupled chloride transport. *Elife* **2019**, *8*, e46986.

26

(17) Chang, Y.-N.; Jaumann, E. A.; Reichel, K.; Hartmann, J.; Oliver, D.; Hummer, G.; Joseph, B.; Geertsma, E. R. Structural basis for functional interactions in dimers of SLC26 transporters. *Nature Communications* **2019**, *10*, 2032.

(18) Yu, X.; Yang, G.; Yan, C.; Baylon, J. L.; Jiang, J.; Fan, H.; Lu, G.; Hasegawa, K.; Okumura, H.; Wang, T.; Tajkhorshid, E.; Li, S.; Yan, N. Dimeric structure of the uracil:proton symporter UraA provides mechanistic insights into the SLC4/23/26 transporters. *Cell Research* **2017**, *27*, 1020–1033.

(19) Wang, W.; Tsirulnikov, K.; Zhekova, H. R.; Kayık, G.; Khan, H. M.; Azimov, R.; Abuladze, N.; Kao, L.; Newman, D.; Noskov, S. Y.; Zhou, Z. H.; Pushkin, A.; Kurtz, I. Cryo-EM structure of the sodium-driven chloride/bicarbonate exchanger NDCBE. *Nature Communications* **2021**, *12*, 5690.

(20) Coudray, N.; L. Seyler, S.; Lasala, R.; Zhang, Z.; Clark, K. M.; Dumont, M. E.; Rohou, A.; Beckstein, O.; Stokes, D. L. Structure of the SLC4 transporter Bor1p in an inward-facing conformation. *Protein Science* **2017**, *26*, 130–145.

(21) Jardetzky, O. Simple allosteric model for membrane pumps. *Nature* **1966**, *211*, 969–970.

(22) Alper, S. L.; Sharma, A. K. The SLC26 gene family of anion transporters and channels. *Molecular aspects of medicine* **2013**, *34*, 494–515.

(23) Long, S. P.; Marshall-Colon, A.; Zhu, X.-G. Meeting the global food demand of the future by engineering crop photosynthesis and yield potential. *Cell* **2015**, *161*, 56–66.

(24) Searchinger, T.; Waite, R.; Hanson, C.; Ranganathan, J.; Matthews, E. *Creating a Sustainable Food Future: A Menu of Solutions to Feed Nearly 10 Billion People by 2050*; 2019.

(25) Hollingsworth, S. A.; Dror, R. O. Molecular Dynamics Simulation for All. *Neuron* **2018**, *99*, 1129–1143.

27

(26) Chan, M. C.; Shukla, D. Markov state modeling of membrane transport proteins. *Journal of Structural Biology* **2021**, *213*, 107800.

(27) Chen, J.; White, A.; Nelson, D. C.; Shukla, D. Role of substrate recognition in modulating strigolactone receptor selectivity in witchweed. *Journal of Biological Chemistry* **2021**, *297*, 101092.

(28) Shukla, S.; Zhao, C.; Shukla, D. Dewetting Controls Plant Hormone Perception and Initiation of Drought Resistance Signaling. *Structure* **2019**, *27*, 692–702.e3.

(29) Moffett, A. S.; Bender, K. W.; Huber, S. C.; Shukla, D. Molecular dynamics simulations reveal the conformational dynamics of Arabidopsis thaliana BRI1 and BAK1 receptor-like kinases. *Journal of Biological Chemistry* **2017**, *292*, 12643–12652.

(30) Zhou, H.; Dong, Z.; Verkhivker, G.; Zoltowski, B. D.; Tao, P. Allosteric mechanism of the circadian protein Vivid resolved through Markov state model and machine learning analysis. *PLOS Computational Biology* **2019**, *15*, e1006801.

(31) Zhao, Y.; Zhang, Y.; Sun, M.; Zheng, Q. A theoretical study on the signal transduction process of bacterial photoreceptor PpSB1 based on the Markov state model. *Physical Chemistry Chemical Physics* **2021**, *23*, 2398–2405.

(32) Trozzi, F.; Wang, F.; Verkhivker, G.; Zoltowski, B. D.; Tao, P. Dimeric allostery mechanism of the plant circadian clock photoreceptor ZEITLUPE. *PLOS Computational Biology* **2021**, *17*, e1009168.

(33) Selvam, B.; Yu, Y.-C.; Chen, L.-Q.; Shukla, D. Molecular Basis of the Glucose Transport Mechanism in Plants. *ACS Central Science* **2019**, *5*, 1085–1096.

(34) Cheng, K. J.; Selvam, B.; Chen, L.-Q.; Shukla, D. Distinct Substrate Transport Mechanism Identified in Homologous Sugar Transporters. *The Journal of Physical Chemistry B* **2019**, *123*, 8411–8418.

(35) Weigle, A. T.; Carr, M.; Shukla, D. Impact of Increased Membrane Realism on Conformational Sampling of Proteins. *Journal of Chemical Theory and Computation* **2021**, *17*, 5342–5357.

(36) Feng, J.; Selvam, B.; Shukla, D. How do antiporters exchange substrates across the cell membrane? An atomic-level description of the complete exchange cycle in NarK. *Structure* **2021**, *29*, 922–933.e3.

(37) Chan, M. C.; Procko, E.; Shukla, D. Structural Rearrangement of the Serotonin Transporter Intracellular Gate Induced by Thr276 Phosphorylation. *ACS Chemical Neuroscience* **2022**, *13*, 933–945.

(38) Selvam, B.; Mittal, S.; Shukla, D. Free Energy Landscape of the Complete Transport Cycle in a Key Bacterial Transporter. *ACS Central Science* **2018**, *4*, 1146–1154.

(39) Beckstein, O.; Naughton, F. General principles of secondary active transporter function. *Biophysics Reviews* **2022**, *3*, 011307.

(40) Drew, D.; Boudker, O. Shared Molecular Mechanisms of Membrane Transporters. *Annual Review of Biochemistry* **2016**, *85*, 543–572.

(41) Matsuoka, R.; Fudim, R.; Jung, S.; Zhang, C.; Bazzone, A.; Chatzikyriakidou, Y.; Robinson, C. V.; Nomura, N.; Iwata, S.; Landreh, M.; Orellana, L.; Beckstein, O.; Drew, D. Structure, mechanism and lipid-mediated remodeling of the mammalian Na+/H+ exchanger NHA2. *Nature Structural & Molecular Biology* **2022**, *29*, 108–120.

(42) Winkelmann, I.; Matsuoka, R.; Meier, P. F.; Shutin, D.; Zhang, C.; Orellana, L.; Sexton, R.; Landreh, M.; Robinson, C. V.; Beckstein, O.; Drew, D. Structure and elevator mechanism of the mammalian sodium/proton exchanger NHE9. *The EMBO Journal* **2020**, *39*, 4541–4559.

(43) Lee, C.; Kang, H. J.; von Ballmoos, C.; Newstead, S.; Uzdavinys, P.; Dotson, D. L.; Iwata, S.; Beckstein, O.; Cameron, A. D.; Drew, D. A two-domain elevator mechanism for sodium/proton antiport. *Nature* **2013**, *501*, 573–577.

(44) Coincon, M.; Uzdavinys, P.; Nji, E.; Dotson, D. L.; Winkelmann, I.; Abdul-Hussein, S.; Cameron, A. D.; Beckstein, O.; Drew, D. Crystal structures reveal the molecular basis of ion translocation in sodium/proton antiporters. *Nature Structural & Molecular Biology* **2016**, *23*, 248–255.

(45) Dong, Y.; Gao, Y.; Ilie, A.; Kim, D.; Boucher, A.; Li, B.; Zhang, X. C.; Orlowski, J.; Zhao, Y. Structure and mechanism of the human NHE1-CHP1 complex. *Nature Communications* **2021**, *12*, 3474.

(46) Ruan, Y.; Miyagi, A.; Wang, X.; Chami, M.; Boudker, O.; Scheuring, S. Direct visualization of glutamate transporter elevator mechanism by high-speed AFM. *Proceedings of the National Academy of Sciences* **2017**, *114*, 1584–1588.

(47) Murata, N.; Wada, H.; Gombos, Z. Modes of Fatty-Acid Desaturation in Cyanobacteria. *Plant and Cell Physiology* **1992**, *33*, 933–941.

(48) Wada, H.; Murata, N. *Lipids in photosynthesis: structure, function and genetics*; Springer, 1998; pp 65–81.

(49) Case, D. A.; Ben-Shalom, I.; Brozell, S.; Cerutti, D.; Cheatham III, T.; Cruzeiro, V.; Darden, T.; Duke, R.; Ghoreishi, D.; Gilson, M.; Gohlke, H.; Goetz, A. W.; Greene, D.; Harris, R.; Homeyer, N.; Huang, Y.; Izadi, S.; Kovalenko, A.; Kurtzman, T.; Lee, T. S.; LeGrand, S.; Li, P.; Lin, C.; Liu, J.; Luchko, T.; Luo, R.; Mermelstein, D. J.; Merz, K. M.; Miao, Y.; Monard, G.; Nguyen, C.; Nguyen, H.; Omelyan, I.; Onufriev, A.; Pan, F.; Qi, R.; Roe, D. R.; Roitberg, A.; Sagui, C.; Schott-Verdugo, S.; Shen, J.; Simmerling, C. L.; Smith, J.; SalomonFerrer, R.; Swails, J.; Walker, R. C.; Wang, J.;

Wei, H.; Wolf, R. M.; Wu, X.; Xiao, L.; York, D. M.; Kollman, P. A. AMBER 2018. *University of California, San Francisco* **2018**,

(50) Klauda, J. B.; Venable, R. M.; Freites, J. A.; OConnor, J. W.; Tobias, D. J.; Mondragon-Ramirez, C.; Vorobyov, I.; MacKerell, A. D.; Pastor, R. W. Update of the CHARMM All-Atom Additive Force Field for Lipids: Validation on Six Lipid Types. *The Journal of Physical Chemistry B* **2010**, *114*, 7830–7843.

(51) van Eerden, F. J.; de Jong, D. H.; de Vries, A. H.; Wassenaar, T. A.; Marrink, S. J. Characterization of thylakoid lipid membranes from cyanobacteria and higher plants by molecular dynamics simulations. *Biochimica et Biophysica Acta (BBA) - Biomembranes* **2015**, *1848*, 1319–1330.

(52) Jumper, J.; Evans, R.; Pritzel, A.; Green, T.; Figurnov, M.; Ronneberger, O.; Tunyasuvunakool, K.; Bates, R.; Žídek, A.; Potapenko, A.; Bridgland, A.; Meyer, C.; Kohl, S. A. A.; Ballard, A. J.; Cowie, A.; Romera-Paredes, B.; Nikolov, S.; Jain, R.; Adler, J.; Back, T.; Petersen, S.; Reiman, D.; Clancy, E.; Zielinski, M.; Steinegger, M.; Pacholska, M.; Berghammer, T.; Bodenstein, S.; Silver, D.; Vinyals, O.; Senior, A. W.; Kavukcuoglu, K.; Kohli, P.; Hassabis, D. Highly accurate protein structure prediction with AlphaFold. *Nature* **2021**, *596*, 583–589.

(53) Shibagaki, N.; Grossman, A. R. Binding of Cysteine Synthase to the STAS Domain of Sulfate Transporter and Its Regulatory Consequences. *Journal of Biological Chemistry* **2010**, *285*, 25094–25102.

(54) Ko, S. B.; Zeng, W.; Dorwart, M. R.; Luo, X.; Kim, K. H.; Millen, L.; Goto, H.; Naruse, S.; Soyombo, A.; Thomas, P. J.; Muallem, S. Gating of CFTR by the STAS domain of SLC26 transporters. *Nature Cell Biology* **2004**, *6*, 343–350.

(55) Jiang, T.; Wen, P.-C.; Trebesch, N.; Zhao, Z.; Pant, S.; Kapoor, K.; Shekhar, M.;

31

616 Tajkhorshid, E. Computational Dissection of Membrane Transport at a Microscopic
617 Level. *Trends in Biochemical Sciences* **2020**, *45*, 202–216.

618 (56) Dror, R. O.; Dirks, R. M.; Grossman, J.; Xu, H.; Shaw, D. E. Biomolecular Simula-
619 tion: A Computational Microscope for Molecular Biology. *Annual Review of Biophysics*
620 **2012**, *41*, 429–452.

621 (57) Husic, B. E.; Pande, V. S. Markov state models: From an art to a science. *Journal of*
622 *the American Chemical Society* **2018**, *140*, 2386–2396.

623 (58) Phillips, J. C.; Hardy, D. J.; Maia, J. D. C.; Stone, J. E.; Ribeiro, J. V.; Bernardi, R. C.;
624 Buch, R.; Fiorin, G.; Hénin, J.; Jiang, W.; McGreevy, R.; Melo, M. C. R.; Radak, B. K.;
625 Skeel, R. D.; Singharoy, A.; Wang, Y.; Roux, B.; Aksimentiev, A.; Luthey-Schulten, Z.;
626 Kalé, L. V.; Schulten, K.; Chipot, C.; Tajkhorshid, E. Scalable molecular dynamics
627 on CPU and GPU architectures with NAMD. *The Journal of Chemical Physics* **2020**,
628 *153*, 044130.

629 (59) Crooks, G. E.; Hon, G.; Chandonia, J.-M.; Brenner, S. E. WebLogo: a sequence logo
630 generator. *Genome research* **2004**, *14*, 1188–1190.

631 (60) Jiang, T.; Wen, P.-C.; Trebesch, N.; Zhao, Z.; Pant, S.; Kapoor, K.; Shekhar, M.;
632 Tajkhorshid, E. Computational dissection of membrane transport at a microscopic level.
633 *Trends in biochemical sciences* **2020**, *45*, 202–216.

634 (61) Babu, M.; Greenblatt, J. F.; Emili, A.; Strynadka, N. C.; Reithmeier, R. A.;
635 Moraes, T. F. Structure of a SLC26 anion transporter STAS domain in complex with
636 acyl carrier protein: implications for E. coli YchM in fatty acid metabolism. *Structure*
637 **2010**, *18*, 1450–1462.

638 (62) Okazaki, K.-i.; Wöhlert, D.; Warnau, J.; Jung, H.; Yildiz, Ö.; Kühlbrandt, W.; Hum-
639 mer, G. Mechanism of the electroneutral sodium/proton antiporter PaNhaP from
640 transition-path shooting. *Nature communications* **2019**, *10*, 1742.

(63) Martínez, L.; Andrade, R.; Birgin, E. G.; Martínez, J. M. PACKMOL: A package for building initial configurations for molecular dynamics simulations. *Journal of Computational Chemistry* **2009**, *30*, 2157–2164.

(64) Webb, B.; Sali, A. Comparative Protein Structure Modeling Using MODELLER. *Current Protocols in Bioinformatics* **2016**, *54*, 5.6.1–5.6.37.

(65) Evans, R.; O'Neill, M.; Pritzel, A.; Antropova, N.; Senior, A.; Green, T.; Žídek, A.; Bates, R.; Blackwell, S.; Yim, J.; Ronneberger, O.; Bodenstein, S.; Zielinski, M.; Bridgland, A.; Potapenko, A.; Cowie, A.; Tunyasuvunakool, K.; Jain, R.; Clancy, E.; Kohli, P.; Jumper, J.; Hassabis, D. Protein complex prediction with AlphaFold-Multimer. *bioRxiv* **2021**, doi:10.1101/2021.10.04.463034.

(66) Hopkins, C. W.; Le Grand, S.; Walker, R. C.; Roitberg, A. E. Long-time-step molecular dynamics through hydrogen mass repartitioning. *Journal of chemical theory and computation* **2015**, *11*, 1864–1874.

(67) Huynh, K. W.; Jiang, J.; Abuladze, N.; Tsirulnikov, K.; Kao, L.; Shao, X.; Newman, D.; Azimov, R.; Pushkin, A.; Zhou, Z. H.; Kurtz, I. CryoEM structure of the human SLC4A4 sodium-coupled acid-base transporter NBCe1. *Nature Communications* **2018**, *9*, 900.

(68) Roe, D. R.; Cheatham, T. E. PTRAJ and CPPTRAJ: Software for Processing and Analysis of Molecular Dynamics Trajectory Data. *J. Chem. Theory Comput.* **2013**, *9*, 3084–3095.

(69) McGibbon, R.; Beauchamp, K.; Harrigan, M.; Klein, C.; Swails, J.; Hernndez, C.; Schwantes, C.; Wang, L.-P.; Lane, T.; Pande, V. MDTraj: A Modern Open Library for the Analysis of Molecular Dynamics Trajectories. *Biophys. J* **2015**, *109*, 1528–1532.

(70) Humphrey, W.; Dalke, A.; Schulten, K. VMD: visual molecular dynamics. *Journal of molecular graphics* **1996**, *14*, 33–38.

(71) Zhou, Q.; Yang, D.; Wu, M.; Guo, Y.; Guo, W.; Zhong, L.; Cai, X.; Dai, A.; Jang, W.; Shakhnovich, E. I.; Liu, Z.-J.; Stevens, R. C.; Lambert, N. A.; Babu, M. M.; Wang, M.-W.; Zhao, S. Common activation mechanism of class A GPCRs. *eLife* **2019**, *8*, e50279.

(72) Shirts, M. R.; Chodera, J. D. Statistically optimal analysis of samples from multiple equilibrium states. *The Journal of chemical physics* **2008**, *129*, 124105.

(73) Ashkenazy, H.; Abadi, S.; Martz, E.; Chay, O.; Mayrose, I.; Pupko, T.; Ben-Tal, N. ConSurf 2016: an improved methodology to estimate and visualize evolutionary conservation in macromolecules. *Nucleic acids research* **2016**, *44*, W344–W350.